Rapid Evolution of Volatile CO from the Protostellar Disk Stage to the Protoplanetary Disk Stage

Ke Zhang[1,3] , Kamber R. Schwarz[2,4] , and Edwin A. Bergin[1]

[1] Department of Astronomy, University of Michigan, 323 West Hall, 1085 South University Avenue, Ann Arbor, MI 48109, USA; kezhang@umich.edu
[2] Lunar and Planetary Laboratory, University of Arizona, 1629 East University Boulevard, Tucson, AZ 85721, USA

Abstract

Recent observations show that the CO gas abundance, relative to H_2, in many 1–10 Myr old protoplanetary disks may be heavily depleted by a factor of 10–100 compared to the canonical interstellar medium (ISM) value of 10^{-4}. When and how this depletion happens can significantly affect compositions of planetesimals and atmospheres of giant planets. It is therefore important to constrain whether the depletion occurs already at the earliest protostellar disk stage. Here we present spatially resolved observations of $C^{18}O$, $C^{17}O$, and $^{13}C^{18}O$ $J = 2-1$ lines in three protostellar disks. We show that the $C^{18}O$ line emits from both the disk and the inner envelope, while $C^{17}O$ and $^{13}C^{18}O$ lines are consistent with a disk origin. The line ratios indicate that both $C^{18}O$ and $C^{17}O$ lines are optically thick in the disk region, and only the $^{13}C^{18}O$ line is optically thin. The line profiles of the $^{13}C^{18}O$ emissions are best reproduced by Keplerian gaseous disks at similar sizes as their mm-continuum emissions, suggesting small radial separations between the gas and mm-sized grains in these disks, in contrast to the large separation commonly seen in protoplanetary disks. Assuming a gas-to-dust ratio of 100, we find that the CO gas abundances in these protostellar disks are consistent with the ISM abundance within a factor of 2, nearly one order of magnitude higher than the average value of 1–10 Myr old disks. These results suggest that there is a fast, $\sim$1 Myr, evolution of the abundance of CO gas from the protostellar disk stage to the protoplanetary disk stage.

1. Introduction

Circumstellar disks around young stars set the stage for planet formation (Williams & Cieza 2011). The chemical composition of natal disks may change dramatically from the formation of disks in embedded protostars to the time of disk gas dispersal several Myr later. These changes will profoundly affect the compositions of planets formed at different disk locations and timescales.

One particularly surprising discovery regarding the composition of disk material is that the abundance of volatile gas-phase CO in many protoplanetary disks (1–10 Myr old, Class II) may be one or two orders of magnitude lower than the canonical value. First, significant CO depletion (by a factor of 5–100) was found in all three protoplanetary disks that have independent gas mass measurements from HD (1-0) line fluxes (Favre et al. 2013; Kama et al. 2016; McClure et al. 2016; Schwarz et al. 2016; Trapman et al. 2017; Zhang et al. 2017). Moreover, surprisingly weak CO emissions are seen in the majority of Class II disks in nearby star formation regions, even after correcting the effects of CO freeze-out and isotope-selective photodissociation (Ansdell et al. 2016; Miotello et al. 2016; Long et al. 2017; Zhang et al. 2019). This weak CO problem can be explained either by more than one order of magnitude of CO depletion, or by a rapid gas dissipation. But a gas-rich condition (gas-to-dust ratio $\sim$100) is required to explain mass accretion rates of these disks (Manara et al. 2016) and to match the observed outer edges of mm-dust emission with that predicted by dust drifting models (Powell et al. 2019).

These results all point to significant CO depletion in many Class II disks.

It is still unclear when and how the CO gas depletion happens. Theoretical works suggest that the abundance of CO gas in the disk atmosphere can be reduced either by chemical processes that turn CO into other less volatile carbon species (Bergin et al. 2014; Eistrup et al. 2016; Bosman et al. 2018; Schwarz et al. 2018, 2019), or by dust growth processes that sequester CO ice into the disk midplane (Xu et al. 2017; Krijt et al. 2018). Current models require 1 Myr or longer time to reduce the CO gas abundance by a factor of 10 under typical conditions in Class II disks.

It is of particular interest to determine whether CO gas is already depleted at the youngest disk stage (Class 0/I), <1 Myr, as growing number of observations suggest the first steps of planet formation may already start at the protostellar disk stage (ALMA Partnership et al. 2015; Zhang et al. 2015; Harsono et al. 2018). Rapid evolution of CO gas abundance will lead to significant variations in the carbon inventory of planetesimals and atmospheres of giant planets formed at different timescales.

Measuring the abundance of CO gas in protostellar disks is challenging due to line confusion from the surrounding envelopes and outflows. There have been few observational constraints of CO abundances attributed to the disk alone, and existing ones gave conflicting results. On the inner envelope scale ($\sim$1000 au), $C^{18}O$ (2−1) images of four Class 0 sources suggest significant CO depletion (Anderl et al. 2016), but *Herschel*-HIFI observation of high J (up to $J = 10$) CO transitions of deeply embedded low-mass Class 0/I systems do not show depletion (Yıldız et al. 2013). Scaling down to the disk region, fluxes of $C^{18}O$ (2−1) line from the HL Tau and V2775 Ori disks suggest gas-to-dust mass ratios of <10, which

---

[3] Hubble Fellow.
[4] Sagan Fellow.

potentially implies a factor of 10 depletion in CO abundance (Yen et al. 2017; Zurlo et al. 2017). However, even $C^{18}O$ lines can be optically thick in protostellar disks (van't Hoff et al. 2018). A more robust way is to employ rarer CO isotopologue lines (e.g., $C^{17}O$, $^{13}C^{18}O$, $^{13}C^{17}O$) that have smaller optical depths (Zhang et al. 2017; Artur de la Villarmois et al. 2018; Booth et al. 2019; Booth & Ilee 2020).

Here we report spatially resolved observations of $C^{18}O/C^{17}O/^{13}C^{18}O$ (2−1) lines toward three young protostellar disks (<1 Myr). Our goal is to measure the CO gas abundance in the disk area and to test whether it evolves significantly from the protostellar disk stage to the protoplanetary disk stage.

2. Observations

Our protostellar sample consist of three sources: the TMC1A, HL Tau, and DG Tau systems, all with known large Keplerian rotating disks (>100 au, Isella et al. 2010; ALMA Partnership et al. 2015; Aso et al. 2015; Harsono et al. 2018). We chose these large protostellar disks so that these disks and their inner envelopes can be spatially resolved with NOEMA C or D configurations.

The observations were carried out with the NOEMA interferometer between 2017 November and 2019 April. The total on-source integration time was 7.3, 5.4, and 5.3 hr for HL Tau, TMC1A, and DG Tau, respectively. All observations used the new wide-band correlator PolyFix with an instantaneous dual-polarization coverage of 15.5 GHz bandwidth at a fixed resolution of 2000 kHz. In addition, higher spectral resolution chunks were set at the line centers of ^{13}CO, $C^{17}O$, and $^{13}C^{18}O$ (2−1) with a resolution of 65 kHz. The baseline lengths were between 24 and 704 m. Nearby quasars were observed between science targets to calibrate the complex antenna gains. The absolute flux calibrations were obtained by observing MWC 349 and/or LKHA 101. Data calibration and imaging were done using the GILDAS software. We re-binned data to a channel width of 0.5 km s^{-1} to enhance signal-to-noise ratios. After uniform weighting, the synthesized beams are $1{.}''4 \times 1{.}''2$ for TMC1A and DG Tau, and $2{.}''3 \times 1{.}''7$ for HL Tau. The noise levels are 4.6 mJy beam^{-1} in individual channels. The absolute flux uncertainty is expected to be 15%–20% and all 1.3 mm continuum fluxes were consistent with literature values within 15%.

The three isotopologue CO lines were detected in all targets. Figure 1 shows the integrated line emission and velocity maps of the CO lines. The $C^{18}O$ line emissions are generally from $10''$ to $15''$ wide regions and show complicated velocity structures from both disks and surrounding inner envelopes. The $C^{17}O$ and $^{13}C^{18}O$ line emissions are much more compact and centered on the area traced by the dust thermal continuum. Their velocity maps are consistent with position angles of the continuum emission and perpendicular to known outflow/jet in each system. The compact emitting regions and velocity maps suggest that $C^{17}O$ and $^{13}C^{18}O$ line emissions are primarily arising from within the protostellar disk. In Table 2, we list line fluxes integrated from a $5'' \times 5''$ box region. The integrated fluxes of $C^{18}O$ and $C^{17}O$ lines increase with box sizes, but the fluxes of $^{13}C^{18}O$ line do not change as the emissions are compact.

To estimate the optical depth of different lines, we measured ratios of surface brightness temperature (T_b) among three lines at regions where $^{13}C^{18}O$ emission is greater than 3σ. We found

that the $T_b(C^{18}O)/T_b(C^{17}O) \sim 1$ and $T_b(C^{17}O)/T_b(^{13}C^{18}O)$ between 5 and 12. In all cases, line ratios are less than the local interstellar medium (ISM) abundance ratios of $^{18}O/^{17}O = 3.6$ and $^{12}C/^{13}C = 69$ (Wilson 1999). These lower ratios suggest that $C^{18}O$ is highly optically thick and $C^{17}O$ is marginally optically thick ($\tau \sim 2$–3) within these disks. Therefore, we use optically thin $^{13}C^{18}O$ line spectra to measure the CO gas masses.

3. Methods

3.1. Model Setup

Assuming the $^{13}C^{18}O$ line emission is dominantly from the protostellar disk, we adopt a parameterized disk model to derive the CO gas abundances in these disks. The global surface density is from the self-similar solution of a viscously evolving disk (Lynden-Bell & Pringle 1974):

$$\Sigma(R) = \Sigma_c \left(\frac{R}{R_c}\right)^{-\gamma} \exp\left[-\left(\frac{R}{R_c}\right)^{2-\gamma}\right], \quad (1)$$

where Σ_c is the surface density at the characteristic radius R_c, and γ is the gas surface density exponent.

The disk model includes three mass components—gas, a population of small dust, and a population of large dust. The small and large dust populations are assumed to be 5% and 95% of the total solid mass, respectively. Previous observations indicated that significant dust growth and settling may already occur in Class 0/I disks (Pinte et al. 2016; Harsono et al. 2018). The two dust populations are employed to mimic these effects. The gas and the small grain population are assumed to be spatially coupled and characterized by a scale height distribution of $H_g(r) = H_0(r/r_0)^{1.2}$. The large grain population is more settled and has a scale height reduced by a factor of χ, i.e., $H = \chi H_g$ with $\chi < 1$. We use $\chi = 0.1$ for the HL Tau disk, because observations showed that mm-sized dust in this disk is extremely settled (Pinte et al. 2016). For other two disks, we adopt $\chi = 0.2$, a value widely used in literature. Both dust populations are assumed to follow the power-law size distribution of $n(a) \propto a^{-3.5}$ with a minimum grain size of $a_{\min} = 0.005\,\mu m$ and $a_{\max} = 1\,\mu m$ for the small grain population and $a_{\max} = 1$ mm for the large grain population.

The disk size of the large (∼mm-sized) dust population can be constrained by spatially resolved (sub)mm continuum observations, but disk sizes of gas and small grains are more uncertain. In this regard, many Class II disks show that their CO gas disk is much larger than the continuum emission (Ansdell et al. 2018), which is usually attributed to inward radial drift of mm-sized grains (Birnstiel & Andrews 2014; Trapman et al. 2019). Here we start with models that all three components have the same radial surface density profile. We will show later that larger gas disks become inconsistent with our observations of CO line profiles.

For the CO abundance structure, we use a setup similar to Williams & Best (2014). The CO gas abundance is assumed to be a constant across the whole disk region except for the regions cooler than the CO freeze-out temperature (20 K) and above the photodissociation layer. This layer is referred to as the "warm molecular layer" as described by Aikawa et al. (2002). We note that even within this layer the CO gas abundance may vary with location in the disk due to chemical and physical processes (Zhang et al. 2019), but our observations do not have sufficient spatial resolution to constrain these
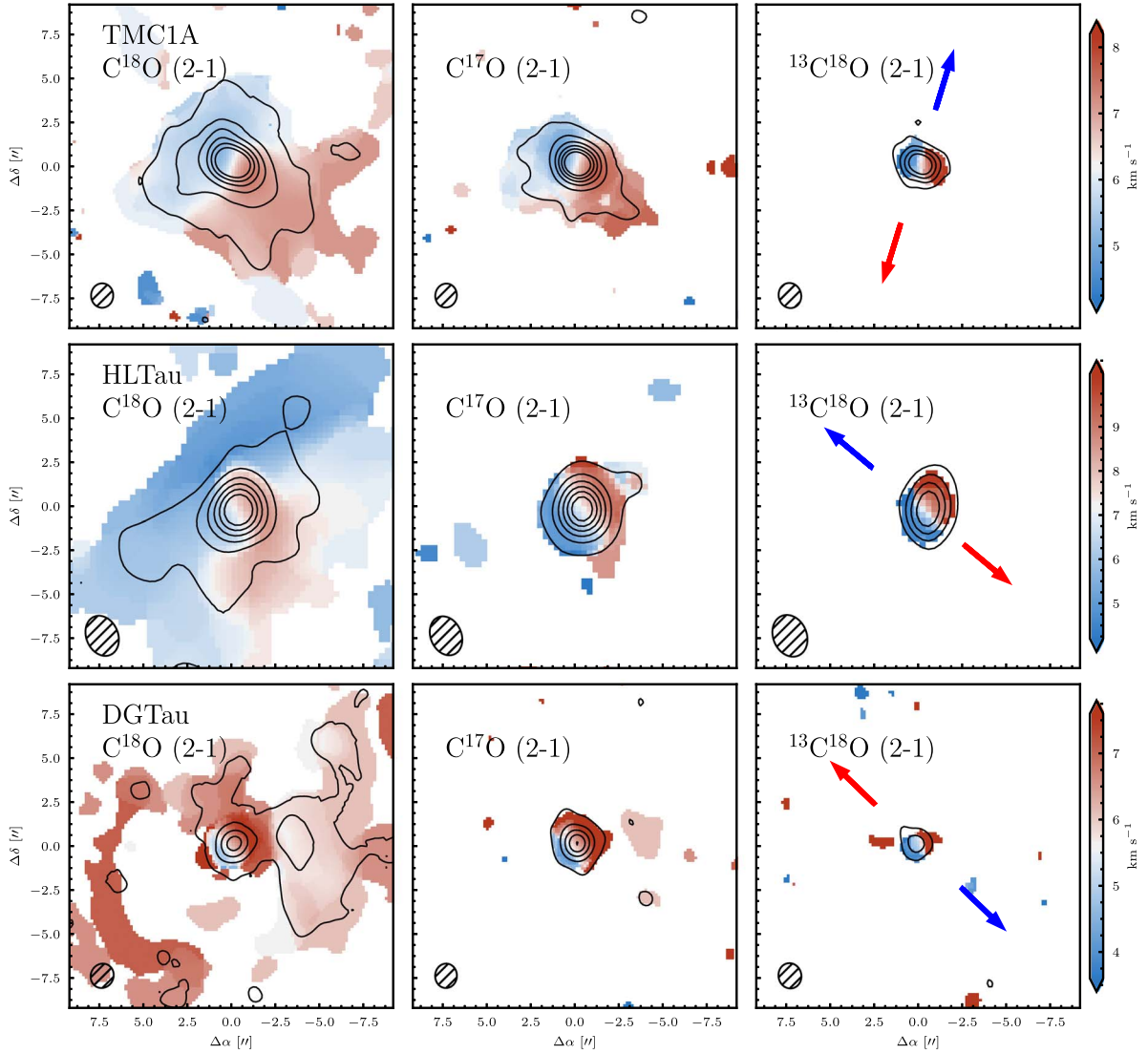
Figure 1. Observations of CO isotopologue (2−1) lines toward TMC1A, HL Tau, and DG Tau systems. The integrated line intensity maps are plotted in contours and the velocity maps are in color. For all lines, contours start at the 3σ level on the integrated images, and increase with 3σ interval for $^{13}C^{18}O$, and with 10σ interval for the $C^{18}O$ and $C^{17}O$ lines. The position angles of known outflows/jets of the three systems are indicated in $^{13}C^{18}O$ panels.

Table 1
Source Information

Source	$M_\star$ $(M_\odot)$	T_{eff} (K)	L_{bol} $(L_\odot)$	M_{disk} $(M_\odot)$	Distance (pc)	Incl (deg)	Disk Position Angle (PA) (deg)	Outflow PA (deg)	Type
TMC1A	0.53	4000	2.5	0.05	140	55	67	−17	Class I
HL Tau	1.7	4000	11	0.13	140	46.2	138.2	50	Class I/II
DG Tau	0.7	4775	6.4	0.02	121	41	120	226	Class I/II

variations. In our model photodissociation is assumed to happen above the $N_{H_2} \sim 10^{21}$ cm^{-2} layer.

We use the radiative transfer code RADMC3D to calculate the thermal structure of the disk (Dullemond et al. 2012). The stellar mass and luminosity are adopted from Table 1. We do not consider viscous heating as it is expected to mostly affect the inner 10 au (Harsono et al. 2015). Gas and dust temperatures are assumed to be the same, as expected for the $^{13}C^{18}O$ line-emitting region (Zhang et al. 2017). We first adopt dust masses from literature and then adjust the masses to match with 1.3 mm continuum fluxes. All of the adjustments are within 20% of the initial values. The gas-to-dust mass ratio is

assumed to be 100, which is expected for protostellar disks and we will discuss the uncertainty of the total disk mass later. We then run a grid of models starting from a CO-to-H$_2$ abundance of 10^{-6}–10^{-3}, increasing by a factor of 1.1 at each step. We then compare the grid of models with the observed spectra of $^{13}C^{18}O$ line to find the best-fit CO abundance for each disk. These results are used to find an initial best-fit CO abundance, and then a finer grid with an increasing step of 1.02 is computed around the initial best-fit value to calculate uncertainties.

We also test a second group of models by setting the gas disk to be a factor of two larger than the dust disk. The choice of a
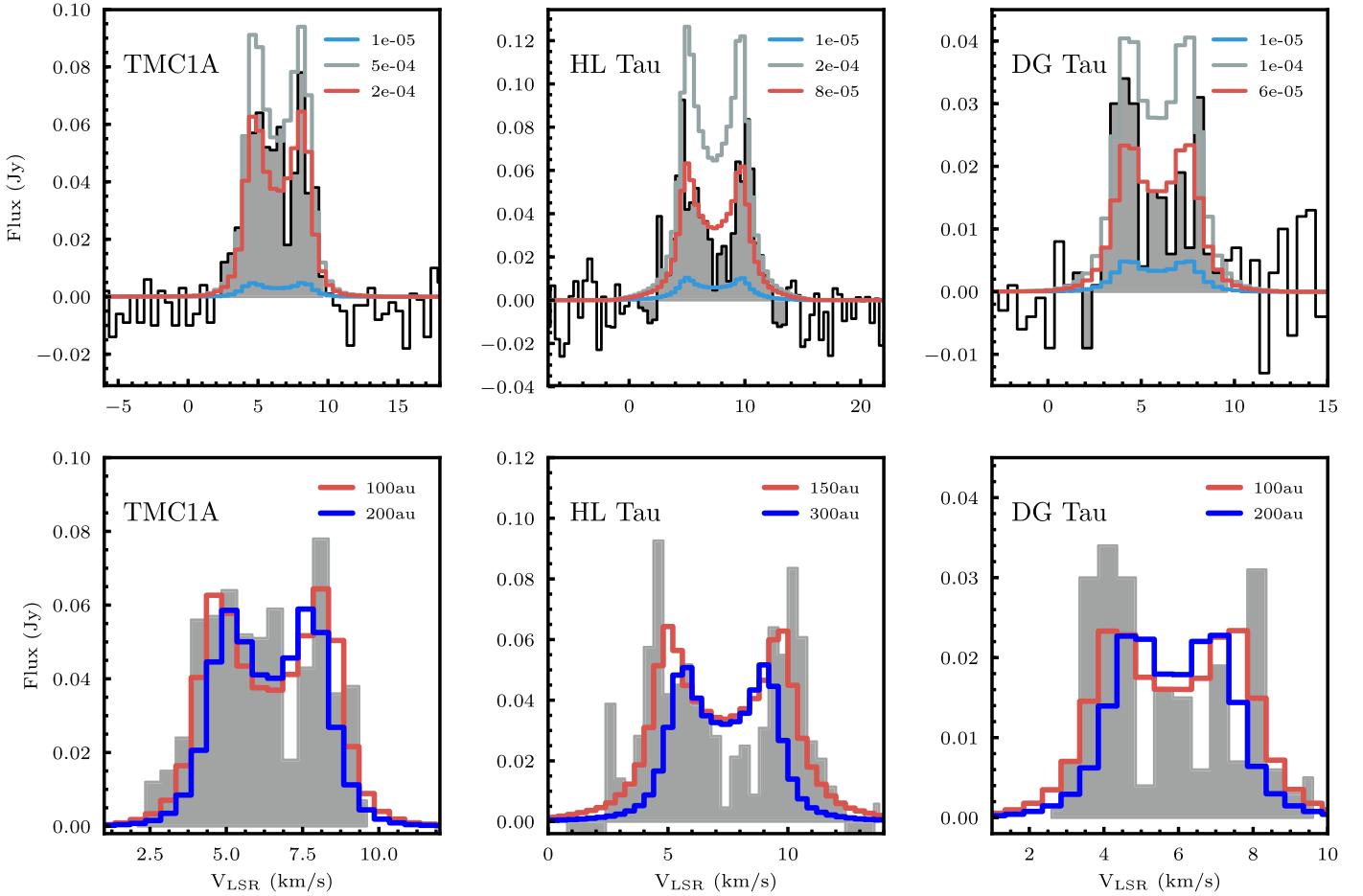
Figure 2. Integrated line profiles of observed $^{13}C^{18}O$ (2−1) line (gray) compared with model spectra. Top row: models of different CO abundances. Models of best-fit abundances, twice of the best-fit abundances, and a CO abundance of 10^{-5} are plotted in red, light gray, and blue, respectively. These results show that the CO gas abundances in the three disks should be 5–20 times higher than the 10^{-5} value seen in many Class II disks. Bottom row: models of the same disk sizes of gas and mm-dust are in red, and models of gas disks twice the size of dust disks are in blue.

Table 2
Line Fluxes and Best-fit CO Abundance

Source	$C^{18}O$ (2−1) (mJy km s^{-1})	$C^{17}O$ (2−1) (mJy km s^{-1})	$^{13}C^{18}O$ (2−1) (mJy km s^{-1})	$F_{1.3\ mm}$ (mJy)	n_{CO}/n_{H_2}
TMC1A	4954 ± 50	3307 ± 48	306 ± 30	183 ± 8	$2.1^{+0.1}_{-0.2} \times 10^{-4}$
HL Tau	3195 ± 69	3357 ± 75	329 ± 37	752 ± 10	$6.7^{+0.6}_{-0.5} \times 10^{-5}$
DG Tau	872 ± 33	781 ± 36	107 ± 27	351 ± 11	$4.6^{+0.4}_{-0.4} \times 10^{-5}$

factor of two is based on the typical size ratio of the CO gas-to-(sub)mm continuum disks seen in Class II disks (Ansdell et al. 2018). The goal is to test if the $^{13}C^{18}O$ line emission is from a much larger radial region than the (sub)mm continuum disk, due to the radial drift of dust, like seen in many Class II disks.

3.2. Model Results

Our first model group has the same disk sizes for both the gas and dust. Its best-fit CO abundances are presented in Figure 2 and Table 2. We find that the CO gas abundances in the warm molecular layer of the three protostellar disks are between 5×10^{-5} and 2×10^{-4}, which is consistent with the canonical ISM value within a factor of 2. These abundances are nearly an order of magnitude higher than that of the majority of Class II disks.

For the second group of models (the gas disk is a factor of two larger than the mm-dust disk), we find that the velocity separations of two peaks of $^{13}C^{18}O$ line profiles become too small to be consistent with observations (see Figure 2). This suggests that the sizes of the CO gas disks are comparable to the continuum disks, which is different from the cases of many Class II disks.

3.3. Uncertainty of CO Abundances

Table 2 shows that the CO abundances in our best-fit models have uncertainties on the level of 10% for the given gas masses. However, the absolute values depend on gas disk masses, and therefore the abundance uncertainties are dominated by uncertainties in gas masses. In our models, we derive gas masses based on the mm-continuum fluxes and assume a gas-to-dust mass ratio of 100, as expected for the very young

(<1 Myr old) protostellar disks. As our dust masses only include masses from grains up to mm-size, we might underestimate the total solid masses and subsequently the gas masses. However, the total disk masses in our models are already 3%–10% of the masses of the central protostars (see Table 1). If the disk masses were 10 times higher, then these disks would be gravitationally unstable and show large-scale spiral structures in their (sub)mm continuum emissions (Pérez et al. 2016). However, none of these disks show significant asymmetric substructures in their high-resolution Atacama Large Millimeter/submillimeter Array (ALMA) continuum observations. It is therefore unlikely that the actual gas masses are 10 times higher than our models, and the ISM level CO abundances derived here cannot be attributed to the uncertainty of gas mass alone.

Detailed dust evolution models of one of our sample disks, the HL Tau disk, requires a gas-to-dust ratio of 50 to match with continuum observations (Tapia et al. 2019). Using the line flux of $^{13}C^{17}O$ (3−2) and a disk-averaged temperature of 25 K, Booth & Ilee (2020) derived a total gas mass of 0.2 $M_\odot$ for the HL Tau disk, which is 1.5 times higher than the gas mass that we use. Based on these independent estimations, we estimate that the uncertainties of our CO abundances are within a factor of 2.

3.4. Sample Selection Bias

Our study of CO abundance in protostellar disks is a small sample and biased to sources with known large Keplerian disks. So far there is no complete survey of the size and mass distribution of Keplerian rotating disks around Class 0/I sources. But our sample is most likely among the largest and most massive protostellar disks, as they are the most easily observable.

One way to evaluate the statistical significance of our results is to compare our sample with the most massive Class II disks. Ansdell et al. (2016) studied 89 Class II disks in the Lupus region and showed that nine out of the top 10 most massive disks (based on dust mass) have CO abundance depletion by a factor of ⩾5 compared to the canonical value. Similarly, Long et al. (2017) studied 93 Class II disks in the Chamaeleon I region and found that eight out of the 10 most massive disks have a factor of ⩾5 depletion in their CO gas abundance. We calculated a Kolmogorov–Smirnov test for the CO abundances of our sample and these of the top 10% most massive disks in the Lupus and Chamaeleon regions. The result shows that there is only a 1.7% probability that these two samples are drawn from the same distribution. Therefore, within the largest and most massive disk population, our results suggest that the CO gas abundance in protostellar disks is significantly higher (by a factor of 5–10) than that in protoplanetary disks.

4. Discussions

4.1. Rapid Evolution of the CO Gas Abundance

We show that three protostellar disks (⩽1 Myr) have CO gas abundances consistent with the ISM abundance within a factor of two. As shown in Figure 3, these CO abundances are nearly one order of magnitude higher than the average values of protoplanetary disks. If these CO abundances are representative of protostellar disks <1 Myr, then there are two important implications: first, the CO gas depletion seen in 1–10 Myr disks are results of processes that occurred inside disks rather than

the infalling envelopes; second, the process is extremely efficient—it depletes volatile CO gas by a factor of 10 within 1 Myr. The timescale of the CO depletion process therefore is comparable with the general timescale of planetesimal/planet formation (Kruijer et al. 2014). Whatever mechanism(s) drive the CO depletion, it can significantly affect the final compositions of planets.

Our measurement of CO gas abundances in protostellar disks are one order of magnitude higher than those measured in the warm inner envelops of four Class 0 sources (Anderl et al. 2016). One way to reconcile these results is that the low CO abundances in the envelopes are due to CO freezing out onto water ice or CO_2 ices, instead of pure CO ice. The sublimation temperatures of these mixed CO ices are 10–15 K higher than that of the pure CO ice (Cleeves et al. 2014).

Our measurements put tight constraints on the timescale of the CO depletion. Because the stellar photosphere of DG Tau is more exposed than for the other two sources, DG Tau is the most evolved source (∼1 Myr) in our sample. However, the majority of disks in Lupus and Cha I (2–3 Myr) already show CO depletion by a factor of 10–100. This rapid change suggests that once the CO depletion process begins, it is a really efficient process.

4.2. CO Depletion Mechanisms

The CO depletion in Class II disks is generally attributed to two types of processes: chemical processes that turn CO into less volatile molecules, and/or dust growth processes that sequester CO ice into the disk midplanes. In the following, we discuss implications of our results for both types of processes.

Current chemical models indicate that an ISM level cosmic-ray ionization rate (10^{-17} s^{-1}) is essential for the chemical processing of CO (Reboussin et al. 2015; Yu et al. 2016; Bosman et al. 2018; Eistrup et al. 2018; Schwarz et al. 2018, 2019). But it is still unclear whether the cosmic-ray ionization rate can reach that high of a level in 1–10 Myr old protoplanetary disks (Cleeves et al. 2015). On the other hand, the cosmic-ray rate might be orders of magnitude higher in protostellar disks due to accretion shocks (Padovani et al. 2016).

Temperature is another important parameter for the efficiency of the CO chemical processing. Given sufficient ionization, chemical models show that the processing occurs most efficiently at 15–30 K (Bosman et al. 2018; Schwarz et al. 2018). This temperature range works the best because the main pathways of CO processing are via CO reactions with OH or H on grain surfaces to form CO_2 or CH_3OH generally. The efficiency of these processes depends on both the amount of CO freeze-out and the speed of reactions on grain surface. Higher temperatures reduce the freeze-out of CO onto grain surfaces, while lower temperatures reduce the efficiency of some grain surface reactions. Depending on the disk structure, chemical processing can work in some regions of protostellar disks.

Chemical models with an ISM cosmic-ray rate generally require 1–3 Myr to achieve a CO depletion by a factor of 10, which is too slow compared to the evolution timescale seen in Figure 3. If the cosmic-ray rate can reach 10^{-16} s^{-1} or higher as predicted by Padovani et al. (2016), the depletion timescale can be shortened to less than 1 Myr.

The second type of mechanism is dust growth, which sequesters CO ice into the midplane. It requires that dust
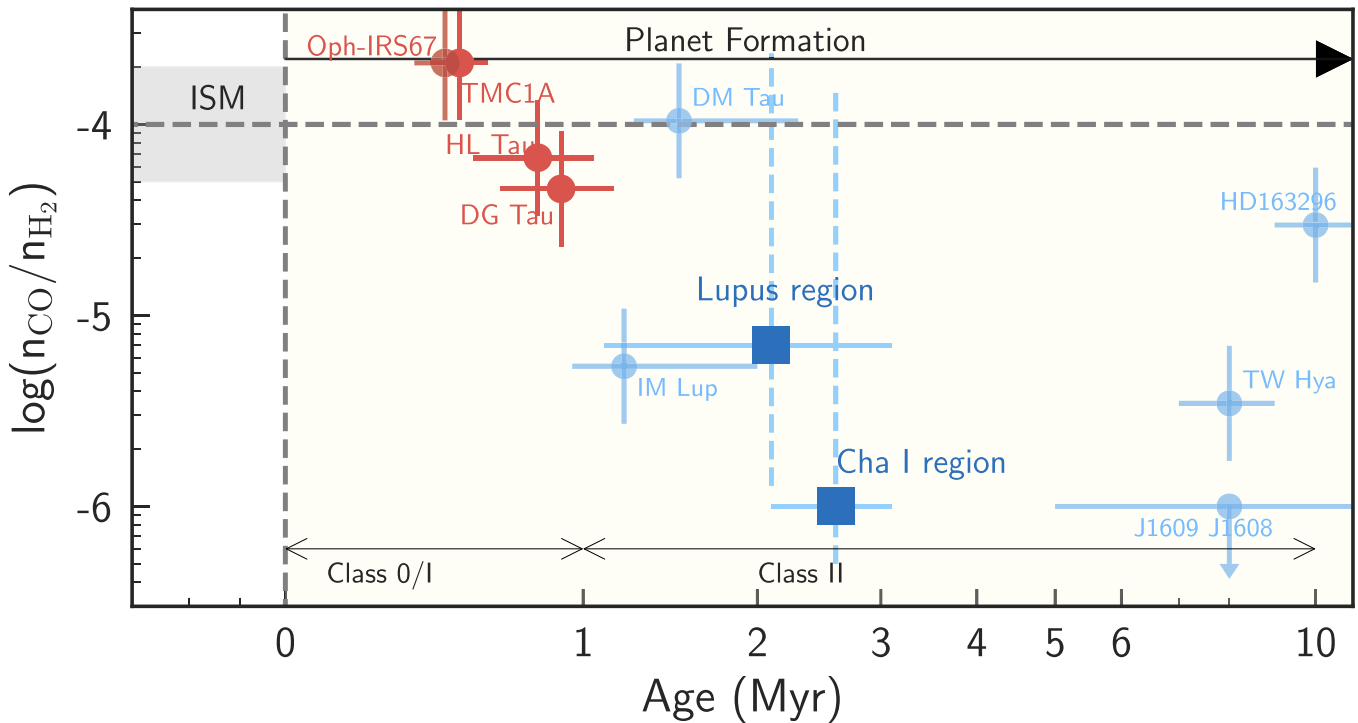
Figure 3. CO gas abundance measurements in protostellar and protoplanetary disks. The protostellar disks (<1 Myr) and protoplanetary disks (1–10 Myr) are in red and blue, respectively. The filled circles are for individual disks and the squares for averaged values of star formation regions. For individual sources, the error bars indicate the expected uncertainties. For star formation regions, dashed lines indicate the full ranges of CO abundances found in each region. The TMC1A, HL Tau, and DG Tau data are from this work, and the Oph-IRS67 from Artur de la Villarmois et al. (2018). The DM Tau, IM Lup, HD 163296, and TW Hya data are from disk average CO abundances of Zhang et al. (2019). The J160900–190852 and J160823–193001 data point is from Anderson et al. (2019). The data of Lupus and Chamaeleon I region are from Ansdell et al. (2016) and Long et al. (2017), respectively. The relative ages of the protostellar systems are based on their spectral energy distribution (SED) shapes (Robitaille et al. 2007). All data assumed a gas-to-dust mass ratio of 100.

growth is ongoing beyond the midplane CO snowline (Krijt et al. 2018). Protostellar disks are expected to be warmer than protoplanetary disks due to their higher accretion luminosity and surrounding envelopes (Harsono et al. 2015). In our models, the CO snowlines are beyond the mm disks in HL Tau and DG Tau, and beyond 60 au in TMC1A. If the disk is warmer than the CO condensation temperature in most of its mass region, little CO would be depleted even if significant dust growth already occurs. This is most clearly seen in the HL Tau disk. It has substantial dust growth into mm- to cm-sized particles, but its disk-averaged abundance of the CO gas is nearly the ISM value.

In summary, the ISM level CO abundances measured in protostellar disks indicate that no more than half of the initial CO gas is depleted at the earliest stage. Dust growth at this stage cannot efficiently deplete the CO abundance due to the lack of CO freeze-out under the warm disk condition. Chemical processing can still be at work if sufficient ionization is provided, and thus may play an important role at the beginning of the CO depletion processes. But the known chemical paths of CO processing also become inefficient in regions warmer than 30 K (Bosman et al. 2018). To explain the fast evolution of the CO abundance, a coupling of physical and chemical processing may be necessary to accelerate the depletion processes.

4.3. Comparing Radii of Gas and Dust Emissions of Protostellar Disks

The emitting radii of (sub)mm-continuum and CO lines of protoplanetary disks typically appear to differ by a factor of 2

or more (Andrews et al. 2012; Ansdell et al. 2018). This discrepancy is often attributed to fast radial drift of dust grains into the inner disk region (Birnstiel & Andrews 2014; Trapman et al. 2019). In our models of the three protostellar disks, we find that models with similar disk sizes of gas and mm-sized dust can better reproduce the observations than that with disk size separations. The lack of size difference can be attributed to neither a lack of dust growth nor a timescale problem. All three disks are known to have a significant amount of dust growth into mm or larger sizes, and dust growth models show that the dust and gas disks can differ by a factor of 2 within 10^5 yr (Birnstiel & Andrews 2014). The lack of size difference hints that the retention of mm-sized dust particles in protostellar disks can be different from protoplanetary disks. For example, Bae et al. (2015) showed that protostellar infall can trigger the Rossby wave instability and form vortices that efficiently trap dust particles in prostellar disks.

4.4. CO as a Gas Mass Tracer of Protostellar Disks

The determination of masses of gas-rich disks around young stars is crucial for nearly all aspects of planet formation. So far, HD is the most robust gas mass tracer, but it has only been detected in three protoplanetary disks and is challenging to be used for protostellar disks. Low J-lines of HD ($J = 1, 2$) emit at far-infrared wavelengths (>50 μm), where the dust emission of the envelope is strong and optically thick.

Given the relatively narrow range of CO gas abundances seen in protostellar disks, we propose that CO may still be a good mass tracer in warm protostellar disks. This is consistent with current theoretical expectation that CO processing through

dust growth does not work in warm regions without CO gas freeze-out. Future investigations of the usage of CO as gas mass tracer would require spatially resolved observations of CO isotopologue lines to evaluate the contribution of disk and envelope and observations of other chemical tracers to evaluate the chemical processing of CO. Observing $^{13}C^{18}O$ low J-lines in ~10 warm protostellar disks with <50 au resolution would be sufficient to test the robustness of CO as a gas mass tracer.

Facility: NOEMA(PolyFix).

Software: RADMC3D (Dullemond et al. 2012), GILDAS,[5] astropy (Astropy Collaboration et al. 2013).

ORCID iDs

Ke Zhang ● https://orcid.org/0000-0002-0661-7517
Kamber R. Schwarz ● https://orcid.org/0000-0002-6429-9457
Edwin A. Bergin ● https://orcid.org/0000-0003-4179-6394

References

Aikawa, Y., van Zadelhoff, G. J., van Dishoeck, E. F., & Herbst, E. 2002, A&A, 386, 622
ALMA Partnership, Brogan, C. L., Pérez, L. M., et al. 2015, ApJL, 808, L3
Anderl, S., Maret, S., Cabrit, S., et al. 2016, A&A, 591, A3
Anderson, D. E., Blake, G. A., Bergin, E. A., et al. 2019, ApJ, 881, 127
Andrews, S. M., Wilner, D. J., Hughes, A. M., et al. 2012, ApJ, 744, 162
Ansdell, M., Williams, J. P., Trapman, L., et al. 2018, ApJ, 859, 21
Ansdell, M., Williams, J. P., van der Marel, N., et al. 2016, ApJ, 828, 46
Artur de la Villarmois, E., Kristensen, L. E., Jørgensen, J. K., et al. 2018, A&A, 614, A26
Aso, Y., Ohashi, N., Saigo, K., et al. 2015, ApJ, 812, 27
Astropy Collaboration, Robitaille, T. P., Tollerud, E. J., et al. 2013, A&A, 558, A33
Bae, J., Hartmann, L., & Zhu, Z. 2015, ApJ, 805, 15
Bergin, E. A., Cleeves, L. I., Crockett, N., & Blake, G. A. 2014, FaDi, 168, 61
Birnstiel, T., & Andrews, S. M. 2014, ApJ, 780, 153
Booth, A. S., & Ilee, J. D. 2020, MNRAS Letters, 493, L108
Booth, A. S., Walsh, C., Ilee, J. D., et al. 2019, ApJL, 882, L31
Bosman, A. D., Walsh, C., & van Dishoeck, E. F. 2018, A&A, 618, A182
Cleeves, L. I., Bergin, E. A., Alexander, C. M. O., et al. 2014, Sci, 345, 1590
Cleeves, L. I., Bergin, E. A., Qi, C., Adams, F. C., & Öberg, K. I. 2015, ApJ, 799, 204
Dullemond, C. P., Juhasz, A., Pohl, A., et al. 2012, RADMC-3D: A Multipurpose Radiative Transfer Tool, v0.41, Astrophysics Source Code Library, ascl:1202.015
Eistrup, C., Walsh, C., & van Dishoeck, E. F. 2016, A&A, 595, A83
Eistrup, C., Walsh, C., & van Dishoeck, E. F. 2018, A&A, 613, A14
Favre, C., Cleeves, L. I., Bergin, E. A., Qi, C., & Blake, G. A. 2013, ApJL, 776, L38
Harsono, D., Bjerkeli, P., van der Wiel, M. H. D., et al. 2018, NatAs, 2, 646
Harsono, D., Bruderer, S., & van Dishoeck, E. F. 2015, A&A, 582, A41
Isella, A., Natta, A., Wilner, D., Carpenter, J. M., & Testi, L. 2010, ApJ, 725, 1735
Kama, M., Bruderer, S., van Dishoeck, E. F., et al. 2016, A&A, 592, A83
Krijt, S., Schwarz, K. R., Bergin, E. A., & Ciesla, F. J. 2018, ApJ, 864, 78
Kruijer, T. S., Touboul, M., Fischer-Gödde, M., et al. 2014, Sci, 344, 1150
Long, F., Herczeg, G. J., Pascucci, I., et al. 2017, ApJ, 844, 99
Lynden-Bell, D., & Pringle, J. E. 1974, MNRAS, 168, 603
Manara, C. F., Rosotti, G., Testi, L., et al. 2016, A&A, 591, L3
McClure, M. K., Bergin, E. A., Cleeves, L. I., et al. 2016, ApJ, 831, 167
Miotello, A., van Dishoeck, E. F., Kama, M., & Bruderer, S. 2016, A&A, 594, A85
Padovani, M., Marcowith, A., Hennebelle, P., & Ferrière, K. 2016, A&A, 590, A8
Pérez, L. M., Carpenter, J. M., Andrews, S. M., et al. 2016, Sci, 353, 1519
Pinte, C., Dent, W. R. F., Ménard, F., et al. 2016, ApJ, 816, 25
Powell, D., Murray-Clay, R., Pérez, L. M., Schlichting, H. E., & Rosenthal, M. 2019, ApJ, 878, 116
Reboussin, L., Wakelam, V., Guilloteau, S., Hersant, F., & Dutrey, A. 2015, A&A, 579, A82
Robitaille, T. P., Whitney, B. A., Indebetouw, R., & Wood, K. 2007, ApJS, 169, 328
Schwarz, K. R., Bergin, E. A., Cleeves, L. I., et al. 2016, ApJ, 823, 91
Schwarz, K. R., Bergin, E. A., Cleeves, L. I., et al. 2018, ApJ, 856, 85
Schwarz, K. R., Bergin, E. A., Cleeves, L. I., et al. 2019, ApJ, 877, 131
Tapia, C., Lizano, S., Sierra, A., Carrasco-González, C., & Bayona-Bobadilla, E. 2019, ApJ, 887, 244
Trapman, L., Facchini, S., Hogerheijde, M. R., van Dishoeck, E. F., & Bruderer, S. 2019, A&A, 629, A79
Trapman, L., Miotello, A., Kama, M., van Dishoeck, E. F., & Bruderer, S. 2017, A&A, 605, A69
van't Hoff, M. L. R., Tobin, J. J., Harsono, D., & van Dishoeck, E. F. 2018, A&A, 615, A83
Williams, J. P., & Best, W. M. J. 2014, ApJ, 788, 59
Williams, J. P., & Cieza, L. A. 2011, ARA&A, 49, 67
Wilson, T. L. 1999, RPPh, 62, 143
Xu, R., Bai, X.-N., & Öberg, K. 2017, ApJ, 835, 162
Yen, H.-W., Takakuwa, S., Chu, Y.-H., et al. 2017, A&A, 608, A134
Yıldız, U. A., Kristensen, L. E., van Dishoeck, E. F., et al. 2013, A&A, 556, A89
Yu, M., Willacy, K., Dodson-Robinson, S. E., Turner, N. J., & Evans, N. J., II 2016, ApJ, 822, 53
Zhang, K., Bergin, E. A., Blake, G. A., Cleeves, L. I., & Schwarz, K. R. 2017, NatAs, 1, 0130
Zhang, K., Bergin, E. A., Schwarz, K., Krijt, S., & Ciesla, F. 2019, ApJ, 883, 98
Zhang, K., Blake, G. A., & Bergin, E. A. 2015, ApJL, 806, L7
Zurlo, A., Cieza, L. A., Williams, J. P., et al. 2017, MNRAS, 465, 834

---

[5] See http://www.iram.fr/IRAMFR/GILDAS for more information about the GILDAS softwares.